Int J Fract (2015) 194:149–167
DOI 10.1007/s10704-015-0045-y

ORIGINAL PAPER

Capturing material toughness by molecular simulation: accounting for large yielding effects and limits

Laurent Brochard · György Hantal · Hadrien Laubie · Franz-Joseph Ulm · Roland J. M. Pellenq

Received: 27 April 2015 / Accepted: 30 September 2015 / Published online: 17 October 2015

Abstract The inherent computational cost of molecular simulations limits their use to the study of nanometric systems with potentially strong size effects. In the case of fracture mechanics, size effects due to yielding at the crack tip can affect strongly the mechanical response of small systems. In this paper we consider two examples: a silica crystal for which yielding is limited to a few atoms at the crack tip, and a nanoporous polymer for which the process zone is about one order of magnitude larger. We perform molecular simulations of fracture of those materials and investigate in particular the system and crack size effects. The simulated systems are periodic with an initial crack. Quasi-static loading is achieved by increasing the system size in the direction orthogonal to the crack while maintaining a constant temperature. As expected, the behaviors of the two materials are significantly different. We show that the behavior of the silica crystal is reasonably well described by the classical framework of linear elastic fracture mechanics (LEFM). Therefore, one can easily upscale engineering fracture properties from molecular simulation results. In contrast, LEFM fails capturing the behavior of the polymer and we propose an alternative analysis based on cohesive crack zone models. We show that with a linear decreasing cohesive law, this alternative approach captures well the behavior of the polymer. Using this cohesive law, one can anticipate the mechanical behavior at larger scale and assess engineering fracture properties. Thus, despite the large yielding of the polymer at the scale of the molecular simulation, the cohesive zone analysis offers a proper upscaling methodology.

Keywords Molecular simulation · LEFM · Large yielding · Cohesive zone

L. Brochard (✉)
Laboratoire Navier (UMR 8205), CNRS, ENPC, IFSTTAR, Université Paris-Est, 77455 Marne-la-Vallée, France
e-mail: laurent.brochard@enpc.fr

G. Hantal · H. Laubie · F.-J. Ulm · R. J. M. Pellenq
Department of Civil and Environmental Engineering, Massachusetts Institute of Technology, 77 Massachusetts Avenue, Cambridge, MA 02139, USA

G. Hantal
Department of Computational Physics, University of Vienna, Sensengasse 8, 1090 Vienna, Austria

1 Introduction

A common issue in mechanical engineering is the material fracture failure, which has to be accounted for carefully for the safety of structures. It is well-known in fracture mechanics that the presence of cracks in a material induces stress concentrations that greatly affect the maximum loading capacity of the material. According to linear elastic fracture mechanics (LEFM), the stress field is singular at crack tips and its asymptotic form when approaching a tip is characterized by the stress intensity factor. LEFM predicts that a crack propagates when the stress intensity factor exceeds a critical value, called toughness. LEFM was very successful at predicting the failure of mechanical structures, even

though the physical existence of infinite stresses at the tip is of course questionable and one expects yielding of the material close to the tip. Actually, as long as the structure considered is much larger than the process zone (small scale yielding assumption), the approximation of LEFM is reasonably valid and this theory predicts correctly the mechanical behavior (Anderson 2005). However, when the size of the process zone is no more negligible compared to the size of the structure, LEFM fails to predict the structure's failure. Theories were developed to capture the effect of yielding at the crack tip, e.g., HRR singularity (Hutchinson 1968) or cohesive zone models (Dugdale 1960; Barenblatt 1962), in which the criterion of crack propagation is no more the toughness (e.g., critical J-integral or the crack tip opening displacement). Those theories are equivalent to usual LEFM under the assumption of small scale yielding, and all the failure criteria are thus related.

The size of the process zone varies widely depending on the material, from Angströms for cleavage fracture of monocrystals to centimeters for concrete and rocks (Bazant 1984). Any measurement of the toughness of a sample for which the process zone size is not negligible should account for yielding effects. This is particularly true when considering molecular simulations approaches since the studied system sizes barely exceed a few tens of nanometers. More fundamentally, a question that arises at the nanoscale is whether continuum fracture mechanics still applies at this scale. For instance, in their early work, Thomson et al. (1971) have shown that the discrete nature of matter at the atomic scale leads to a lattice trapping of the crack, an effect unknown in continuum fracture mechanics. Likewise, a great deal of research efforts was devoted to various atomic scale peculiarities of fracture mechanics: competition between crack propagation and dislocation emissions (Rice and Thomson 1974; Celis et al. 1983; Cheung and Yip 1994), role of inter-atomic potentials (Sinclair 1975; Holian and Ravelo 1995; Marder 2004; Buehler and Gao 2006), role of phonons (Holian and Ravelo 1995; Zhou et al. 1996; Gumbsch et al. 1997), crack velocity (Marder and Gross 1995; Buehler and Gao 2006), dynamic instability (Marder and Gross 1995; Abraham and Broughton 1998; Buehler and Gao 2006; Kermode et al. 2008), effects of crystal orientation and grain boundaries (Miller et al. 1998; Abraham and Broughton 1998; Pérez and Gumbsch 2000), effect of chemical environment and impurities (Lawn 1983; Kermode et al. 2013). A long standing issue in atomic scale studies is the size effect that may arise at such small scales. Holland and Marder (1999) designed a molecular simulation approach and analysis for silicon that is scale insensitive, provided the simulated system is large enough (strip at least 80 atoms high). Bouchbinder et al. (2010) discussed in detail various origins of scale effects that cause deviations from LEFM theory, such as non-linear elasticity and irreversibility at crack tip, potential energy corrugation at the atomic scale, energy flow near the tip. In all cases, LEFM limitations arise from the assumption of continuum linear elasticity at the crack tip. Apart from the intrinsic limitations of continuum theories, material properties are also size dependent when considering nanoscale systems. In particular, the high resistance to fracture of tough materials involves processes that range from breaking of atomic bonds to the nucleation of voids, crazing, crystal rotations or microcracking on the micron and larger scales (Bazant 1984; Garrison and Moody 1987; Anderson 2005; Ward and Sweeney 2012). The toughness of systems smaller than the range of those processes are size dependent. For brittle crystals with process zones a few atoms large, size effects appear for systems a few nanometer large (Nazmus Sakib and Adnan 2012); whereas size effects are at the scale of civil engineering structures for building materials (Bazant 1984). The toughness can also depend on the crack size because of surface energy changes with strain, lattice trapping, and non-linear mechanical behaviors (Mattoni et al. 2005; Zhang et al. 2007). That is, the scale at which the effect of crack size appears is very dependent on the nature of the material.

Although molecular simulation approaches can capture the atomic details of fracture mechanisms, these simulations do not exceed a few billions of atoms with supercomputers and highly efficient implementation (Abraham et al. 2002), which amounts to structures 0.1 μm large. Accordingly, effects due to small sizes are a recurring issue when considering molecular simulation. For fracture studies, the assumption of small scale yielding often fails which is responsible for discrepancies between molecular simulation results and LEFM. In this work, we present an approach to analyze molecular simulation results in order to capture the fracture toughness of materials while accounting for large yielding. This approach is based on cohesive zone models, developed originally by Dugdale (1960) and Barenblatt (1962) to model plastic effect and suppress unphysical stress singularity at crack tips. Cohe-

sive zone models are not the only approach to circumvent the stress singularity of LEFM. Others exists such as the (equivalent) dislocation-based approach (Bilby et al. 1963), the non-local theory (Kröner 1967) and some more recent theories (Pugno and Ruoff 2004; Oh et al. 2006). Since cohesive zone models are known to be inadequate for the modeling of dynamic fracture because of their inherent mathematical formulation (Langer and Lobkovsky 1998), we limit ourselves to quasi-static evolution in this work and disregard crack dynamics. The DBCS analysis ('Dugdale–Bilby–Cottrell–Swinden') of Mattoni et al. (2005) is relevant to the approach developed in this paper. While Mattoni et al. (2005) limited their study to the effect of crack size and analyzed only the critical stress at failure, we consider in this work the system size effect and analyze the complete loading curve.

As case studies, two materials are considered for molecular simulations of fracture. The first one, a silica crystal, is a brittle material for which the process zone is expected to be a few atoms large. The second one, a molecular reconstruction of a saccharose coke, is a highly cross-linked nanoporous polymer which exhibits a significantly larger process zone. Accordingly, the yielding effects should be limited in the first material, but significant in the second, thus providing two complementary cases. For each material, we investigate the effect of system and crack sizes on the fracture behavior, e.g., the critical stress at failure. The molecular simulation results serve as a basis to challenge theories. We identify LEFM strong shortcomings as soon as yielding becomes significant, whereas cohesive zone models proves much more versatile and universal with respect to yielding effect.

In part 2 of this paper, we present the molecular simulations of the two materials considered and illustrate some typical results. In part 3, we propose an analysis that captures the yielding effects by mean of cohesive zone models, and apply it to the two case studies.

2 Molecular simulations

2.1 Simulation details

The design of a molecular simulation is key when considering the simulation of fracture. In particular, major fracture properties such as brittle to ductile transition, crack tip blunting, or crack velocity are very sensitive to small details of the simulation such as the inflection of the attractive part of the inter-atomic potential (Belytschko et al. 2002), the way to handle emitted phonon and dislocations at boundaries (Cheung and Yip 1994), and the loading technique (Holian and Ravelo 1995). With the restriction to quasi-static behaviors, we disregard crack dynamics, and, accordingly, precautions regarding phonon propagation or loading technique are not critical in this work. However, the accuracy of the inter-atomic potential, the choice of boundary conditions and the control of dissipated energy (temperature) are still important issues. Regarding the inter-atomic potential, we use the ReaxFF potential (Duin et al. 2001). ReaxFF is a reactive potential trained on experimental data or quantum calculations results. It has the ability to adapt to various atomic configuration, e.g., for carbon sp, sp2 or sp3 bonds. Therefore, it is able to predict the complex molecular rearrangements that occur in fracture simulations (bond breaking, bond formation, charge transfer etc.). The original version of ReaxFF was parameterized for the simulation of polymers and organic matter. In this work, we use a parameterization of ReaxFF extended to the simulation of silica (Duin et al. 2003; Chenoweth et al. 2005) which is suitable for the two materials we consider in this work. Previous studies on the fracture of silicon have used ReaxFF successfully (Buehler et al. 2006, 2007), and the potential formulation does not seem to exhibit spurious features that would strongly affect the fracture behavior such as the force peak in the REBO reactive potential (Belytschko et al. 2002). In our simulations, the fracture behavior simulated with reaxFF is consistent with the expected materials behaviors: brittle fracture but without cleavage for the silica (Swiler 1994; Swiler et al. 1995), and chain elongation and scission of the nanoporous carbon (Rottler 2009).

In the literature, various boundary conditions are used to model fracture, from clamped boundaries (fixed displacement) (Abraham and Broughton 1998) to prescribed forces on boundary atoms (fixed stress often coupled with continuum mechanics) (Celis et al. 1983) and atoms insertions/removals to follow steady state dynamics (Holland and Marder 1998). A recurring issue is that artificial manipulation of the atom dynamics at the boundary (either by imposing positions or by imposing forces coming from a 'smooth' continuum field) leads to unphysical molecular dynamics in the vicinity of the boundary. When simulating materials near 0 K, which is most often the case in the literature, this issue is of little importance. But in the present work,

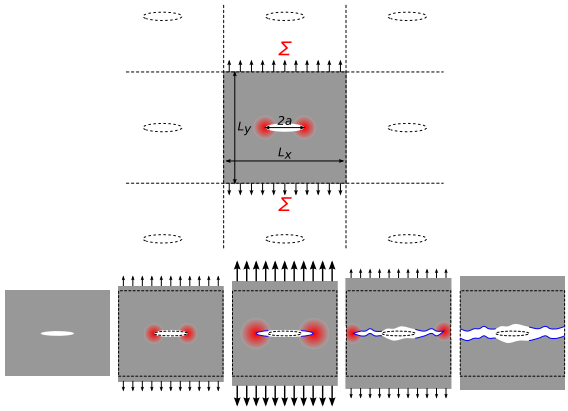

Fig. 1 Schematic representation of the simulated systems. We consider periodic boundary condition and increase the box size to load the system until complete failure. The overall stress Σ is computed

we consider finite temperatures (a key parameter especially for the polymer fracture behavior) and large scale yielding potentially affected by the boundary. Accordingly, spurious effects due to artificial manipulation of boundary atoms are an important issue in this work. To avoid it, we use periodic boundary conditions and control the periodic box size to impose a mechanical loading to the system (see Fig. 1). Periodic boundary conditions mimic an infinite body, do not require to artificially manipulate boundary atoms and avoid surface tensions that arise in non-periodic systems. However, the behavior of a periodic body is not always representative of that of an infinite body (e.g., discrete number of phonon modes). Regarding fracture simulation a recognized issue is the interactions between a crack and its periodic replicas: from a dynamical point of view, the vibrational waves emitted from a crack propagate to the replicas and alter the crack propagation; from a static point of view, the stress intensity at a crack tip is affected by the presence of periodic replicas of the crack. Since we disregard crack dynamics in this work, we are only concerned with the second issue. We properly address this issue in the analysis part.

As mentioned, we perform molecular simulations at room temperature (300 K). Temperature is associated with atom's velocities at the molecular scale, also referred to as 'thermal agitation', which is known to affect the fracture behavior. For instance, the velocity gap phenomenon vanishes upon temperature increase because thermal agitation, on the order of the atomic corrugation of the energy landscape, overcomes the lattice trapping effect (Holland and Marder 1999). Likewise, temperature increase can induce brittle to ductile transition by favoring blunting, dislocation nucleation, or creep (Cheung and Yip 1994). In the present work, temperature is an essential parameter since it strongly affects the mechanics and failure properties of polymers (Rottler 2009; Ward and Sweeney 2012). As an illustration, the strength of the nanoporous polymer we study is two times smaller at room temperature than at 0 K. We use a Nose–Hoover thermostat to impose a temperature of 300 K in our molecular simulation, with a damping parameter of 10 fs (time step of integration 0.1 fs) (Frenkel and Smit 2002). Since the energy dissipation during fracture generates heat, we systematically wait for thermal equilibration after each loading step before acquiring physical observables. Doing so our results can be considered quasi-static.

2.2 Simulation of silica

The first material we consider is α-cristobalite, a silica crystal. Previous molecular simulation studies have investigated the failure behavior of this crystal (Swiler 1994; Swiler et al. 1995). While α-cristobalite is known to exhibit a brittle behavior, cracking does not occur along a specific cleavage plane. Instead, fracture surfaces exhibit fractal character which is typical of silicon oxides (Nakano et al. 1994). We performed molecular simulations of fracture of α-cristobalite by initiating an elliptic crack (aspect ratio 1/5) in the (001) direction of the crystal and by increasing progressively the box size in the direction orthogonal to the cracks. To prepare the initial atomic configurations, we considered the unit cell from Downs and Palmer (1994) ($4.9717 \times 4.9717 \times 6.9223$ Å^3). We considered a total of 24 different situations with various system sizes and initial crack sizes, as listed in Table 1. We display in Fig. 2 some of the systems simulated. The smallest system considered is $29.8 \times 20.8 \times 5.0$ Å^3 large (209 atoms), and the largest $99.4 \times 83.1 \times 19.9$ Å^3 large (11,324 atoms). The smallest crack considered is 7.5 Å long (18 atoms removed) and the largest 50 Å long (548 atoms removed).

To load the system we performed small increments of length of the system in the direction orthogonal to the crack. In a first series of simulations, we increased the length by 1 % every 10 ps, i.e., an equivalent strain rate of 0.001 ps^{-1}. To avoid rate effects, this strain rate is two orders of magnitude smaller than the strain rate

Table 1 Systems considered for simulation of fracture in the (001) plane of α-cristobalite

System	L_x (Å)	L_y (Å)	L_z (Å)	Initial crack size (Å)	Critical stress Σ_{cr} (GPa)
A†	49.72	55.38	14.92	10	19.97
B†	49.72	55.38	14.92	20	15.73
C†	49.72	55.38	14.92	30	10.84
D†	74.58	69.22	24.86	20	14.99
E†	74.58	69.22	24.86	30	11.90
F†	74.58	69.22	24.86	40	9.77
G†	99.43	83.07	19.89	30	12.99
H†	99.43	83.07	19.89	40	10.84
I†	99.43	83.07	19.89	50	7.65
J†	99.43	69.22	4.97	30	12.21
K‡	99.43	69.22	4.97	30	15.92
L‡	89.49	62.30	4.97	30	11.20
M‡	74.58	55.38	4.97	30	10.49
N‡	59.66	41.53	4.97	20	14.24
O‡	49.72	34.61	4.97	20	17.28
P‡	39.77	27.69	4.97	15	15.78
Q‡	29.83	20.77	4.97	12	20.77
R‡	29.83	20.77	14.92	7.46	25.35
S‡	29.83	27.69	14.92	7.46	24.66
T‡	29.83	34.61	14.92	7.46	25.40
U‡	29.83	41.53	14.92	7.46	24.64
V‡	44.75	34.61	14.92	7.46	20.17
W‡	59.66	27.69	14.92	7.46	24.06
X‡	59.66	41.53	14.92	7.46	22.90

† Loading procedure: increments of L_y of 1 % every 10 ps and computation of Σ every 1 fs after a period of equilibration of 5 ps

‡ Loading procedure: increments of L_y of 2.5 % every 2 ps and computation of Σ every 1 fs after a period of equilibration of 1 ps

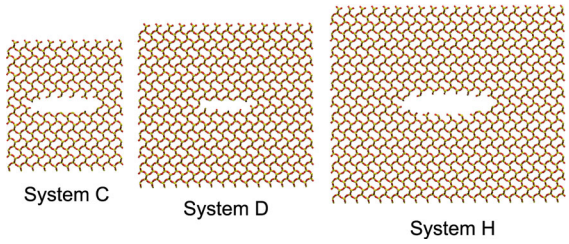

Fig. 2 Three of the systems simulated for α-cristobalite

at which the failure of silica becomes strain rate dependent (Swiler et al. 1995). The average tensile stress in the vertical direction (Σ) was computed every 1 fs after a period of relaxation of the system of 5 ps after each increment. Σ can be interpreted as the average stress on the top and bottom boundary of the periodic cell (Fig. 1) and was computed with the virial equation (Allen and Tildesley 1989). In a second series of simulations, we optimized the loading procedure to reduce the computation time. We considered larger increments (2.5 %) performed more frequently (every 2 ps), corresponding to a strain rate of 0.0125 ps^{-1}, still small enough to prevent any rate effects. Σ was computed every 1 fs after a period of equilibration of 1 ps after each increment. These values were chosen as a good compromise between computational cost and accuracy. All the simulations were performed with the LAMMPS software (Plimpton 1995) (http://lammps.sandia.gov).

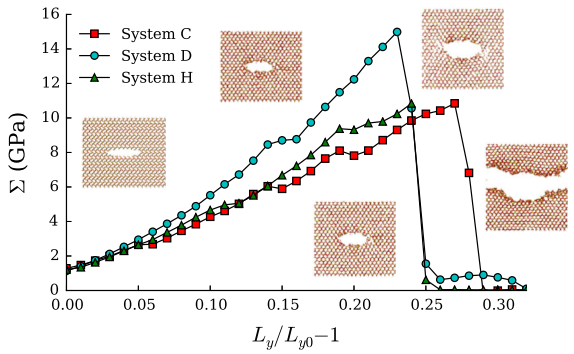

Fig. 3 Results of the molecular simulations for three of the α-cristobalite systems studied. The average tensile stress Σ in the loading direction is represented as a function of the strain imposed to the systems. The snapshots of molecular configurations illustrate the case of system H

In Table 1, we list the critical stress at the onset of failure for all studied systems. In Fig. 3 the full loading curve for the three systems displayed in Fig. 2 are shown. The chart represents the evolution of the average stress Σ as a function of the strain $L_y/L_{y0} - 1$ during the loading procedure up to complete failure (L_{y0} is the initial size of the system). The non-zero stress in the initial state is due to the surface tension induced by the initiated crack and to the reaxFF potential for which the ground state of the material is not exactly that of the initial atomic structure [unit cell from Downs and Palmer (1994)]. We also display on the same figure a few snapshots of the molecular structure for system H that illustrate the different steps of failure. As expected, the mechanical behavior of α-cristobalite is nearly linear elastic up to the onset of crack propagation. The material failure is brittle

with unstable cracking through the whole periodic cell under displacement-controlled loading, leaving behind a rough crack surface. As expected, the critical stress and strain at the onset of failure depend on the crack and system size. In particular, smaller cracks lead to higher critical stresses. The highest critical stress of 25 GPa is obtained for the systems with the smallest crack only 6 atoms long (systems R to X). This value however is still much lower than the yield stress of α-cristobalite (35 GPa, estimated from molecular simulations of bulk α-cristobalite). Therefore, the process zone remains small, typically the size of a few atoms.

2.3 Simulation of nanoporous polymer

The second material we consider is CS1000, a molecular reconstruction of a saccharose-based heat-activated carbon (CS) obtained by Hybrid Reverse Monte Carlo method (Jain et al. 2006). CS1000 is a glassy nanoporous material composed of a highly cross-linked polymeric network (Fig. 4). Fracture mechanisms of polymers are peculiar because of their underlying molecular structure made of chains: chain elongation in the process zone leads to the formation of fibrils bridging the crack faces separated by voids (crazing phenomenon) (Kramer and Berger 1990; Ward and Sweeney 2012). The crazing phenomenon is a strong toughening mechanism: glassy polymers can exhibit fracture energy release rates orders of magnitude larger than their surface energy. Fibrils are typically a few nanometers large and can be studied by molecular simulations; see, for instance, Rottler et al. (2002). In the particular case of CS1000, the high degree of cross-linking strongly limits crazing, since important cross-linking is known to increase the brittleness of polymers (Sauer and Hara 1990). With a high degree of cross-linking, the linear chain structure of polymers is turned into a three-dimensional network which strongly limits the chain mobility, and, therefore, reduces the plastic behavior while increasing the stiffness. Thus, a highly cross-linked polymer exhibits little or no crazing and chain scission is the main failure mechanism. By molecular simulation of bulk CS1000, we estimated the yield strength of the flaw-less matrix to be $\sigma_{YS} = 19$ GPa (high value because of the absence of flaws). We anticipate a toughness of CS1000 in the range of toughness commonly observed for glassy solid polymers, i.e., from 0.5 to 5 MPa $\sqrt{\text{m}}$ (Ashby 2005). Assuming a toughness of $K_{Ic} = 2$ MPa $\sqrt{\text{m}}$, we anticipate a process zone size of $r_p = 4$ nm at the crack tip [following the Dugdale–Barenblatt estimate (Anderson 2005): $r_p = \frac{\pi}{8}\left(\frac{K_{Ic}}{\sigma_{YS}}\right)^2$]. This is a small process zone with respect to polymers in general since process zones associated with crazing can be tens of micrometers large. While the CS1000 process zone is limited in size, it is still about one order of magnitude larger than in the case of silica, which should strongly affect the fracture behavior in our simulation with significant size effects.

An additional complexity of polymer mechanics is the dependency on both temperature and loading rate. When temperature is raised or when loading rate is decreased, amorphous polymers change from glass-like to rubber-like behavior (Ward and Sweeney 2012). In the glassy state, atoms vibrate close to their equilibrium position, whereas in the rubbery state, polymer chains are quite flexible and can adopt a variety of conformations. As a consequence, rubbery polymers, dominated by entropy, are compliant and viscoelastic; while glassy polymers are stiff and elastic. The transition from one regime to another is quite sharp around the glass transition temperature (for a given loading rate). According to the time-temperature equivalence, the viscoelastic behaviour at a temperature is related to the behavior at another temperature by a change in the loading rate only. Following this equivalence, a single master curve fully characterizes the dependence of a polymer mechanical property on both temperature and loading rate. These concepts apply to polymer mechanical failure as well, and master curves for failure properties can be drawn (Smith 1958). In the present case, at room temperature (300 K), CS1000 is well below its glass transition temperature since the heat activation of saccharose at 1000 K removed the most flexible part of the polymer. In addition, the loading rate we consider in this study is high (0.0125 ps^{-1}) because of the

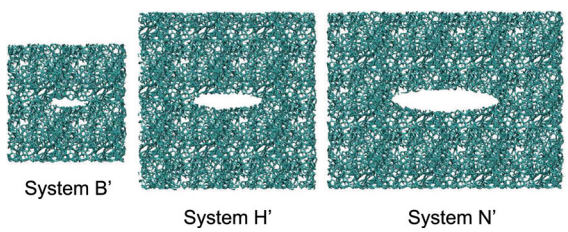

Fig. 4 Three of the systems simulated for CS1000

time scale accessible by molecular simulation. Interestingly, at low temperatures/high loading rates, as is the case here, the time-temperature equivalence master curves are nearly constant, i.e., the properties are temperature and rate independent. Nevertheless, in this work, to avoid any mis-interpretation due to temperature and rate effects, we applied the same temperature and the same loading rate to all CS1000 systems. For one of the systems, we repeated the calculation with a loading rate about one order of magnitude smaller to investigate if significant rate effect could occur.

A series of 15 systems of various sizes constructed from the CS1000 model, with an elliptic crack of various length, but constant aspect ratio (1/5), was considered (detailed characteristics of the systems are listed in Table 2). Three of these systems are displayed in Fig. 4. The systems were loaded by increasing their length orthogonal to the crack by 2.5 % every 2 ps (strain rate of 0.0125 ps^{-1}). The average tensile stress (Σ) in the direction orthogonal to the crack was computed every 1 fs after a period of equilibration of 1 ps after each increment. In addition, we repeated the molecular simulation for system C′ but with a much smaller loading rate of 0.001 ps^{-1} (System P′). The systems were loaded until complete failure was achieved. We report in Table 2 the critical stress at the onset of failure for all the systems simulated, and display in Fig. 5 the average tensile stress Σ as a function of the strain, $L_y/L_{y0}-1$, for the three systems displayed in Fig. 4. In addition, we include in Fig. 5 a few snapshots of molecular configuration for system N′ to illustrate the steps of CS1000 failure. Contrary to α-cristobalite, CS1000 failure is stable upon displacement-controlled loading. One can clearly observe significant yield at the crack tips. As for α-cristobalite, the critical stress and strain at the onset of failure depend on the crack and system size. That is, as expected, the smaller the crack the larger the critical stress. But, in the case of CS1000, the maximum critical stress (15.53 GPa, system A′) is quite close to the yield strength (19 GPa). in fact, for this system, the yielding of the crack plane is almost complete since the uncracked area for this system represents 80 % of the cross section in the crack plane.

Table 2 Systems considered for simulations of fracture in CS1000

System	L_x (Å)	L_y (Å)	L_z (Å)	Initial crack size (Å)	Critical stress Σ_{cr} (GPa)
A′†	50	50	25	10	15.53
B′†	50	50	25	15	14.15
C′†	50	50	25	20	13.83
D′†	50	50	25	25	10.89
E″†	50	50	25	30	9.44
F′†	75	75	25	20	13.52
G′†	75	75	25	25	13.49
H′†	75	75	25	30	11.43
I′†	75	75	25	35	10.63
J′†	75	75	25	40	8.94
K′†	100	75	25	30	12.41
L′†	100	75	25	35	12.57
M′†	100	75	25	40	11.99
N′†	100	75	25	45	9.59
O′†	100	75	25	50	9.31
P′‡	50	50	25	20	12.79

† Loading procedure: increments of L_y of 2.5 % every 2 ps and computation of Σ every 1 fs after a period of equilibration of 1 ps

‡ Loading procedure: increments of L_y of 1 % every 10 ps and computation of Σ every 1 fs after a period of equilibration of 5 ps

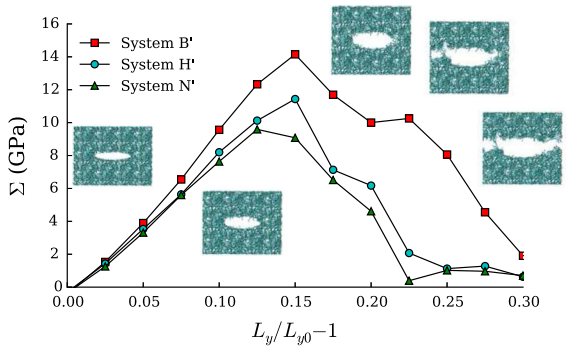

Fig. 5 Results of the molecular simulations for three of the CS1000 systems studied. The average tensile stress Σ in the loading direction is represented as a function of the strain imposed to the systems. The snapshots of molecular configurations illustrate the case of system N′

3 Mechanical analysis

3.1 LEFM analysis

We first consider the strict application of LEFM to the present situation. LEFM assumes linear elasticity

even at the crack tips, a consequence of which is the stress singularity at the tips ($\sigma \propto 1/\sqrt{r}$, where r is the distance from the crack tip). The stress intensity K_I in mode I loading, as is the case here, is defined as $K_I = \lim_{x\to 0^+} \sqrt{2\pi x}\sigma_{yy}\ (y=0)$ for a crack orthogonal to the y direction and for a crack tip located at $(x=0; y=0)$. The stress intensity characterizes the singularity of the stress at the crack tip and depends on the geometry and loading conditions of the system. For instance, for a crack of size $2a$ in an infinite body subjected to a remote stress Σ orthogonal to the crack, the stress intensity is $K_I = \Sigma\sqrt{\pi a}$. Failure occurs when the stress intensity reaches the fracture toughness, K_{Ic}. Therefore, for the finite crack in an infinite body, the critical stress at failure is a function of the crack size $\Sigma_{cr} = K_{Ic}/\sqrt{\pi a}$. For the periodic geometry we consider in this work (Fig. 1), the situation is more complex, since the stress intensity at a crack tip is affected by the presence of the periodic replicas of the crack. By dimensional analysis, the dimensionless reduced stress intensity $K_I/\left(\Sigma\sqrt{\pi a}\right)$ also depends on the dimensionless quantities characterizing the periodic geometry, i.e., L_y/L_x and $2a/L_x$:

$$\frac{K_I}{\Sigma\sqrt{\pi a}} = C_{K_I}\left(\frac{2a}{L_x}, \frac{L_y}{L_x}\right) \tag{1}$$

This specific periodic geometry has been studied within the framework of LEFM (Watanabe and Atsumi 1972; Isida et al. 1981; Karihaloo et al. 1996; Karihaloo and Wang 1997). While there exists no analytical formulation of $C_{K_I}\left(2a/L_x, L_y/L_x\right)$, one can quantify it numerically. In this work, we followed the numerical approach proposed by Karihaloo et al. (1996), which consists in a pseudo-traction method based on the solution of a single periodic array of collinear cracks (Tada et al. 2000). The problem of an infinite body with a doubly periodic array of crack submitted to a remote loading Σ is first decomposed into a homogeneous crack-free problem submitted to the remote loading and a subsidiary problem in which the system is submitted to the loading on the crack faces instead. The subsidiary problem is further decomposed into an infinite number of identical sub-problems where a body with a single row of periodic collinear crack is submitted to pseudo-tractions σ^p on the crack faces. For the second decomposition to be valid, the pseudo-tractions must satisfy the consistency equation:

$$\sigma^p(x) - 2\sum_{j=1}^{+\infty}\int_0^a K_{\sigma j}(x,u)\,\sigma^p(u)\,du = \Sigma \tag{2}$$

where the kernel $K_{\sigma j}(x,u)$ represents the stress induced by the pseudo-traction $\sigma^p(u)$ in the sub-problem with collinear periodic cracks at $y = -jL_y$ at the location of the pseudo-traction $\sigma^p(x)$ in the sub-problem with the collinear periodic cracks at $y=0$. It is readily obtained from the analytic solution for an infinite body with periodic collinear cracks (Tada et al. 2000): $K_{\sigma j}(x,u) = \mathrm{Re}\left(Z\left(x + i\left(jL_y\right), u\right)\right) + jL_y\mathrm{Im}\left(Z'\left(x + i\left(jL_y\right), u\right)\right)$, with $Z' = \frac{dZ}{dz}$ and Z the Westergaard stress function below for collinear periodic cracks problem:

$$Z(z,u) = \frac{2}{L_x}\frac{\cos\left(\frac{\pi u}{L_x}\right)}{\left(\left(\sin\left(\frac{\pi z}{L_x}\right)\right)^2 - \left(\sin\left(\frac{\pi u}{L_x}\right)\right)^2\right)} \times \sqrt{\frac{\left(\sin\left(\frac{\pi a}{L_x}\right)\right)^2 - \left(\sin\left(\frac{\pi u}{L_x}\right)\right)^2}{1 - \left(\sin\left(\frac{\pi a}{L_x}\right)/\sin\left(\frac{\pi z}{L_x}\right)\right)^2}} \tag{3}$$

Karihaloo et al. (1996) solved Eq. 2 by means of a Gauss–Legendre quadrature method in which pseudo-tractions $\sigma^p(x)$ are discretized at the integration points. Once the pseudo-tractions are known, one can easily access any quantity of interest. For instance, the stress intensity results from the pseudo tractions of a single sub-problem (only one sub-problem leads to a singular stress):

$$K_I = \int_0^a K_{K_I}(u)\,\sigma^p(u)\,du \tag{4}$$

with

$$K_{K_I}(u) = \frac{2}{L_x}\frac{\cos\left(\frac{\pi u}{L_x}\right)\sqrt{L_x\tan\left(\frac{\pi a}{L_x}\right)}}{\sqrt{\left(\sin\left(\frac{\pi a}{L_x}\right)\right)^2 - \left(\sin\left(\frac{\pi u}{L_x}\right)\right)^2}} \tag{5}$$

Likewise, the deformation of the periodic cell is obtained by the superposition of the deformations in the homogeneous problem and in all the sub-problems. The displacement Δ of the periodic boundary at $y = L_y/2$ is:

$$\Delta = \frac{L_y}{2}\frac{\Sigma}{E'} + \sum_{j=-\infty}^{+\infty} \int_0^a K_{\Delta j}(u)\, \sigma^p(u)\, du \tag{6}$$

where $K_{\Delta j}(u) = (2/E')\,\mathrm{Im}\left(\overline{Z}\left(i\left(j+\frac{1}{2}\right)L_y, u\right) - \overline{Z}\left(i\left(jL_y\right), u\right)\right)$ and $Z = d\overline{Z}/dz$. E' is the elastic modulus in plane strain, which is the case here: $E' = E/\left(1-\nu^2\right)$, with E the Young's modulus and ν the Poisson's ratio.

We applied the approach of Karihaloo et al. (1996) to account for the interactions between periodic cracks. The values of the correction factor C_{K_I} in Eq. 1 are generally greater than 1, i.e., the influence of the periodic replicas of a crack leads to higher stress intensities than for an infinite body; up to 20 % increase for the geometries we consider in this work. But, for some geometries, e.g. $L_y/L_x < 0.6$ and $2a/L_x < 0.45$, the stress intensity is moderately lower than in the infinite body ($C_{K_I} < 1$) which leads to a toughening of the material. Thus, the effect of the doubly periodic array of crack can be counter-intuitive and needs to be accounted for carefully.

Like the stress intensity, the deformation of the periodic cell is affected by the presence of periodic cracks. The ratio between the dimensionless deformation $\Delta^* = 2\Delta/L_y$ and dimensionless stress $\Sigma^* = \Sigma/E'$ is a function of the dimensionless quantities L_y/L_x and $2a/L_x$ characterizing the periodic geometry, and can be computed from Eq. 6:

$$\frac{2\Delta/L_y}{\Sigma/E'} = C_\Delta\left(\frac{2a}{L_x}, \frac{L_y}{L_x}\right) \tag{7}$$

With these corrections, one can fully characterize the failure behavior as predicted by LEFM. Before failure, the mechanical behavior is linear elastic and follows Eq. 7. Failure occurs when the stress intensity reaches the toughness. The critical stress at the onset of failure is

$$\Sigma_{cr} = \frac{K_{Ic}}{\sqrt{\pi a}\, C_{K_I}\left(\frac{2a}{L_x}, \frac{L_y}{L_x}\right)} \tag{8}$$

Then, in the quasi-static limit, the stress intensity is equal to the toughness all along the crack propagation. Therefore, for any crack length larger than the initial length $a > a_0$, the stress can be obtained from Eq. 8 and the corresponding strain from Eq. 7. We summarize the loading and failure of the periodic system as follows:

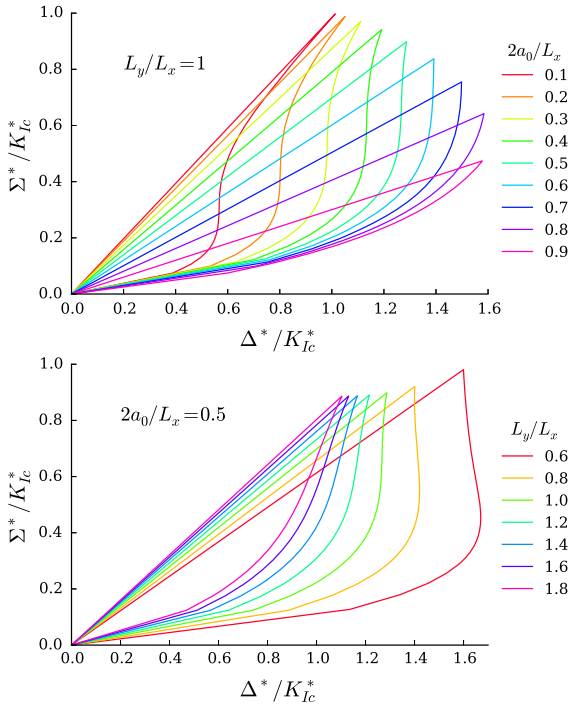

Fig. 6 Loading curves as predicted by LEFM for various crack sizes and periodic cell elongations. We display the dimensionless reduced stress Σ^*/K^*_{Ic} as a function of the dimensionless reduced strain Δ^*/K^*_{Ic}. The behavior is linear elastic until $K_I = K_{Ic}$, i.e., $\Sigma^*/K^*_{Ic} = C_{K_I}\left(\frac{a_0}{L_x}, \frac{L_y}{L_x}\right)$. Then, cracking occurs until complete propagation through the periodic box

$$\left|\begin{array}{l}\text{Before failure, for } a = a_0\\ \frac{\Delta^*}{K^*_{Ic}} = C_\Delta\left(\frac{2a_0}{L_x}, \frac{L_y}{L_x}\right)\frac{\Sigma^*}{K^*_{Ic}} \text{ with } \frac{\Sigma^*}{K^*_{Ic}} < \left(C_{K_I}\left(\frac{2a_0}{L_x}, \frac{L_y}{L_x}\right)\right)^{-1}\\ \text{Then, for } a > a_0\\ \frac{\Delta^*}{K^*_{Ic}} = C_\Delta\left(\frac{2a}{L_x}, \frac{L_y}{L_x}\right)\frac{\Sigma^*}{K^*_{Ic}} \text{ with } \frac{\Sigma^*}{K^*_{Ic}} = \left(\sqrt{\frac{a}{a_0}}C_{K_I}\left(\frac{2a}{L_x}, \frac{L_y}{L_x}\right)\right)^{-1}\end{array}\right. \tag{9}$$

where we introduced the dimensionless reduced strain Δ^*/K^*_{Ic} and the dimensionless reduced stress Σ^*/K^*_{Ic} with $K^*_{Ic} = K_{Ic}/\left(E'\sqrt{\pi a_0}\right)$. Note that after failure the control variable is the crack length a that increases from a_0 to $L_x/2$.

Figure 6 displays the mechanical behavior of the periodic system as predicted by LEFM. It highlights that the behavior depends on the dimension ratios $2a/L_x$ and L_y/L_x. The behavior is linear elastic until the onset of failure, with an elasticity depending on the geometric ratios. Then, failure is almost always unstable upon both stress-controlled loading and displacement-controlled loading. That is, we

almost always have $\frac{d\Sigma^*}{da} < 0$ and $\frac{d\Delta^*}{da} < 0$. This is a peculiarity of the periodic system. In the periodic geometry, when the crack propagates, the tips come closer to their periodic replicas which enhances stress intensity and favors instability. Failure is stable upon displacement loading if $\left.\frac{\partial K_I}{\partial a}\right|_{\Delta} < 0$. For the periodic system, this criterion is verified only for quite elongated systems (L_y/L_x small) and the range of crack length for which failure is stable is limited. The systems we considered are all close to a square geometry. Therefore, we expect unstable failure in our case.

The critical stress at failure (Eq. 8) also differs from the case of an infinite body, because of the correction term C_{K_I}. Equation 8 can be rewritten in the following dimensionless form:

$$\frac{\Sigma^*_{cr}}{\sqrt{G^*_c}} = \left(\sqrt{\pi \frac{2a}{L_x}} C_{K_I}\left(\frac{2a}{L_x}, \frac{L_y}{L_x}\right)\right)^{-1} \tag{10}$$

where we introduced the dimensionless reduced failure stress $\Sigma^*_{cr}/\sqrt{G^*_c}$, with $\Sigma^*_{cr} = \Sigma_{cr}/E'$ and $G^*_c = G_c/\left(\frac{L_x}{2}E'\right)$. G_c is the critical energy release rate and is related to the toughness K_{Ic} according to Irwin's formula (Anderson 2005): $G_c = (K_{Ic})^2/E'$. We display in Fig. 7 the dependence of $\Sigma^*_{cr}/\sqrt{G^*_c}$ on the geometric ratios $2a/L_x$ and L_y/L_x. For small crack sizes ($2a/L_x \to 0$), we recover the critical stress of a finite crack in an infinite body. However, for moderate and large crack sizes ($2a/L_x > 0.2$), the critical stress of a periodic system deviates from that of an infinite system. Particularly large deviations appear for $2a/L_x > 0.5$. In the limit of $2a/L_x \to 1$ the crack tips merge at the periodic boundary, and, accordingly, the critical stress converges to 0. For the systems we simulated, the ratio $2a_0/L_x$ ranges from 0.13 to 0.60. Therefore, accounting for the correction C_{K_I} is necessary in our work to analyze the critical stresses.

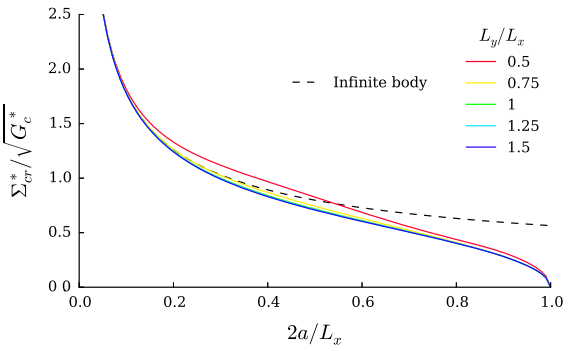

Fig. 7 LEFM prediction of the critical stress at the onset of failure. We display the dimensionless reduced failure stress $\Sigma^*_{cr}/\sqrt{G^*_c}$ as a function of the crack size $2a/L_x$ for different elongations L_y/L_x of the periodic cell. We also display the case of a finite crack in an infinite body: $\Sigma^*_{cr}/\sqrt{G^*_c} = 1/\sqrt{\pi \frac{2a}{L_x}}$. When $2a/L_x \to 0$ one recovers the critical stress of an infinite body. In contrast, significant deviations appears for larger crack sizes, especially for $2a/L_x > 0.5$

3.2 Application of the LEFM analysis to molecular simulation results

We apply the LEFM analysis to the molecular simulation results of α-cristobalite and CS1000. Regarding loading curve shape and failure stability, it is clear that CS1000 results are in contradiction with LEFM prediction: CS1000 failure is stable upon displacement loading, and the loading curves (Fig. 5) exhibit significant ductility with an ultimate strain at the end of failure about twice the critical strain at the onset of failure. In contrast, the α-cristobalite results (Fig. 3) are consistent with LEFM: the behavior is almost linear and failure is unstable since stresses fall to zero right after the onset of failure. In our molecular simulations, it is not possible to follow the instable branches that appear in Fig. 6. Instead, the stress drops to zero at failure.

A quantitative comparison with LEFM theory can be achieved by plotting the critical stress at failure as a function of the effective crack half length $a_{eff} = a\left(C_{K_I}\left(\frac{2a}{L_x}, \frac{L_y}{L_x}\right)\right)^2$. If LEFM theory was respected, following Eq. 8, we would observe that the critical stress is proportional to the inverse of the square root of the effective crack length: $\Sigma_{cr} = K_{Ic}/\sqrt{\pi a_{eff}}$. By fitting the curve, one can recover the fracture toughness K_{Ic} characterizing the material. We display in Fig. 8 the critical stresses obtained for molecular simulations as a function of a_{eff} for all simulated systems. On the same Figure we display the fitted inverse square root dependency according to LEFM theory. For α-cristobalite, the results seem consistent with LEFM. In the Figure, we distinguish between the two loading rates (see Table 1). We do not observe any rate effects, but it appears that the long simulation procedure (smallest rate) provides more accurate results than the short procedure (largest rate) for which the results are significantly more dispersed. Despite the disper-

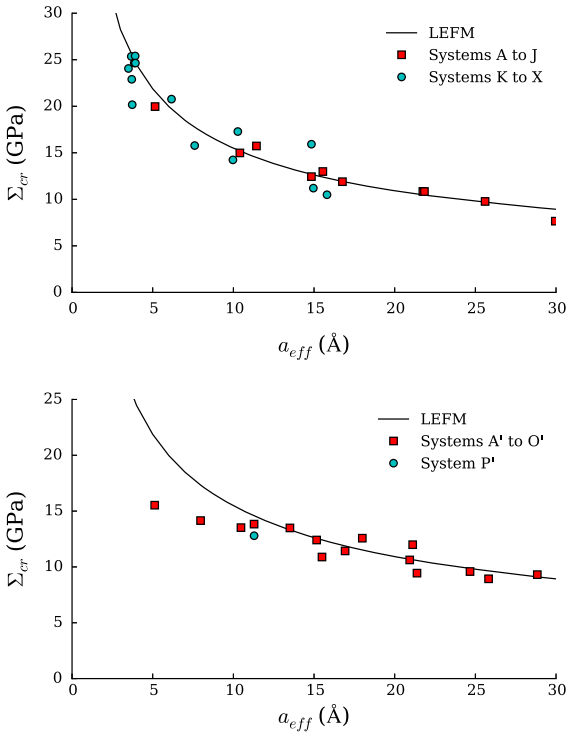

Fig. 8 Critical stress Σ_{cr} obtained from molecular simulation for α-cristobalite (*top*) and CS1000 (*bottom*) as a function of the effective half length of the crack a_{eff}. The results for α-cristobalite respect LEFM theory, whereas the results for CS1000 differ significantly from LEFM at low crack lengths

sion, the results are quite consistent with LEFM theory. The fitting leads to a fracture toughness $K_{Ic} = 0.87$ MPa $\sqrt{\text{m}}$. This value is consistent with experimental values of toughness of silica. Indeed, Lucas et al. (1995) reported $K_{Ic} = 0.82 \pm 0.07$ MPa.m$^{1/2}$. In contrast to α-cristobalite, the results of CS1000 exhibit a rather linear trend with the effective crack length, which is in contradiction with the inverse square root dependency predicted by LEFM. Any tentative application of LEFM to the results for CS1000 leads to serious discrepancies between theory and observation. A tentative application is displayed in Fig. 8 with large discrepancies at low crack lengths; the corresponding toughness is the same as for α-cristobalite ($K_{Ic} = 0.87$ MPa $\sqrt{\text{m}}$).

As an alternative to critical stress, one can focus on the energy released during failure. The critical energy release rate G_c is the energy released during the fracture per unit area of crack surface created. Fracture occurs when the system can release enough mechanical energy P upon cracking, with G_c defining this threshold. Formally, G_c is the variation of mechanical energy $-dP$ due to a small advance of the crack (increment of crack area dA): $G_c = -\frac{\partial P}{\partial A}\big|_{T,\text{loading}}$. Together, G_c and P are the two forms of energy for a system exposed to mechanical loading whose response is limited to deformation or fracture. In isothermal conditions, as is the case here, the balance of Helmholtz free energy F is: $dF = dP + G_c dA$. The average stress Σ is the derivative of the Helmholtz free energy F with respect to the periodic cell size L_y: $\Sigma = \frac{1}{L_x L_z}\frac{\partial F}{\partial L_y}\Big|_{T,L_x,L_z}$. Accordingly, integrating Σ with respect to L_y provides a way to calculate the variation of free energy. In particular the integration of the complete loading curves (Fig. 6) leads to the critical energy release rate. Indeed, at the beginning of the loading curve, the system is unstressed, i.e., $P = 0$; at the end of the loading curve, the system is also unstressed and $P = 0$. Therefore, all the mechanical energy accumulated during the loading was converted into fracture energy at the end of the loading. Accordingly, the change of Helmholtz free energy calculated from the integration $L_x L_z \int_{\text{loading}} \Sigma dL_y$ is equal to the total increase in fracture energy $G_c \Delta A$, where $\Delta A = L_z\,(L_x - 2a_0)$ is the total area of crack created:

$$G_c = \frac{L_x L_z}{\Delta A} \int_{\text{loading}} \Sigma dL_y \tag{11}$$

The critical energy release rate G_c, as obtained from Eq. 11, can be converted into fracture toughness K_{Ic} following Irwin's formula (Anderson 2005): $G_c = (K_{Ic})^2 / E'$. We applied this thermodynamic integration to compute the toughness of α-cristobalite and CS1000 from the molecular simulation results. For α-cristobalite, we obtained an average toughness of 1.13 ± 0.09 MPa $\sqrt{\text{m}}$, which is somewhat higher than the value of 0.87 MPa $\sqrt{\text{m}}$ derived from the critical stress. This discrepancy arises from the fact that integrating the curves of Fig. 3 only provide an overestimation of the critical energy release rate because of instability. Indeed, proper integration should follow the unstable branch that recede to smaller strains when the crack advances (such as in Fig. 6). But, our molecular simulations are unable to follow the unstable branch and instead the stress drops to zero. As a consequence, the integration of stress (area delimited by the loading curve) overestimates the critical energy

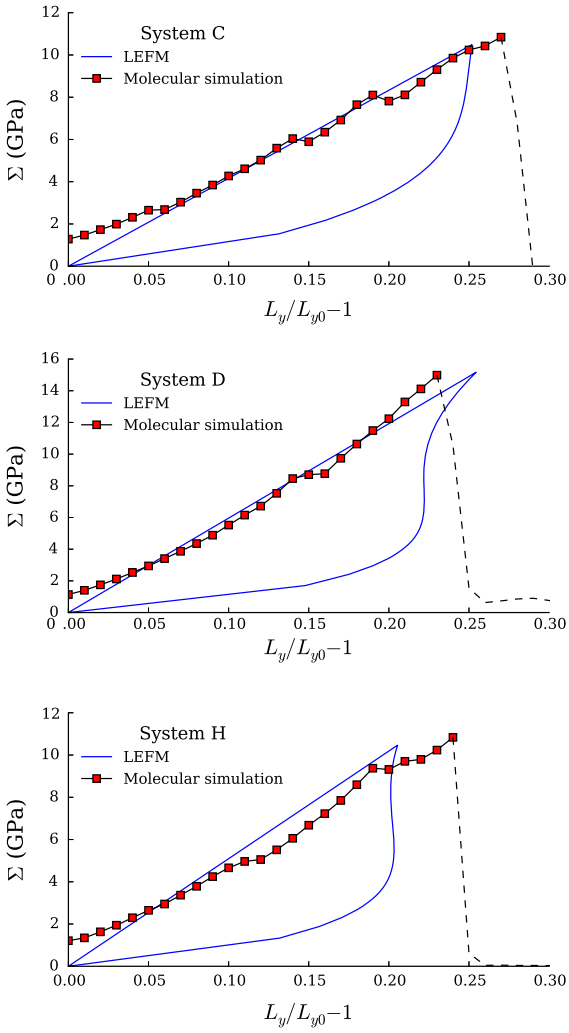

Fig. 9 Loading curves from molecular simulations compared with LEFM predictions for the three systems of Fig. 2

release rates. For CS1000, the same restriction does not apply since failure is stable. The integration of the loading curves for CS1000 leads to an average toughness of 1.49 ± 0.14 MPa $\sqrt{\text{m}}$, i.e., almost twice the value estimates from the critical stress and LEFM. With this toughness, the critical stresses predicted by LEFM would be twice that obtained by molecular simulations. This further confirms that LEFM is invalid for CS1000.

To illustrate the application of LEFM to α-cristobalite, we display in Fig. 9 the loading curves from molecular simulations along with that derived from LEFM, for the three systems of Fig. 2. LEFM captures satisfactorily the elastic behavior and predicts the onset of failure with a reasonable accuracy given the inherent variabilities of the simulations (in particular thermal agitation and variable crack tip initial configuration). The failure branches differ significantly as already discussed above. Figure 9 illustrates well the overestimation of the toughness when performing a thermodynamic integration on the molecular simulation results.

3.3 Cohesive zone analysis

LEFM does not capture the behavior of CS1000 in our molecular simulation. This is due to the important yielding at the scale of our molecular simulations. LEFM is valid only in the limit of small scale yielding, which is clearly not the case for the CS1000 systems we simulated. As a consequence, CS1000 response is ductile without instability at failure and the critical stresses obtained are much smaller than expected from LEFM because of the inherent physical limit of CS1000 yield stress. We propose here to introduce a cohesive zone approach in the mechanical modeling of the periodic system in order to capture the behavior of CS1000. Cohesive zones are a simple modeling of the yield zone at crack tips originally introduced by Dugdale (1960) and Barenblatt (1962) to suppress the unphysical stress singularities at crack tips. The approach is illustrated in Fig. 10. Behind the crack tips, the crack faces are cohesive, i.e., an attractive force p between the faces

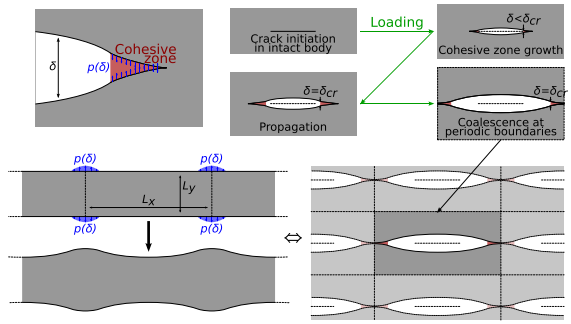

Fig. 10 Schematic representation of the cohesive zone model. Cohesive zones develop behind crack crack tips in which a force is transmitted across the crack, depending on the crack opening. The cohesive zone suppresses the stress singularity at the crack tip. At large openings, the cohesive forces vanish and the crack is unbridged. Loading proceeds in three phases: (1) the cohesive zone grows until the opening at the end of the zone reaches the critical opening, (2) the unbridged crack propagates, (3) the cohesive zones coalesce at the periodic boundaries. In the third phase, the mechanical problem is that of an infinite plate submitted to periodic traction loads on its faces

opposes the opening of the crack. In the original formulation, the cohesive force is constant (plastic stress) and vanishes at a critical opening δ_{cr} of the crack. More generally, the cohesive force p is a function of the opening δ, called the cohesive law. The negative stress intensity at the crack tip due to the cohesive forces cancels out the stress intensity from the external loading so that stress singularity is suppressed. This condition is used to determine the length of the cohesive zone. Failure occurs when the opening at the end of the cohesive zone exceeds the critical opening at which the cohesive force vanishes. Application of the J-integral to a contour following the boundary of the cohesive zone shows that the critical energy release rate is obtained by integration of the cohesive law (Anderson 2005):

$$G_c = \int_0^{\delta_{cr}} p\left(\delta\right) d\delta \tag{12}$$

Thus, one can easily relate the cohesive zone model to usual LEFM. For small scale yielding, the cohesive zone is extremely small compared to the dimensions of the system, in particular the size of the crack. In that case, cohesive zone models and LEFM are strictly equivalent and the two approaches are related by Eq. 12. When yielding becomes significant, cohesive zone predictions differ from that of LEFM. In particular, the stresses cannot exceed the yield stress, the main physical contradiction of LEFM.

Even though cohesive zone models are an idealization of the process zone, they are quite versatile and have been used to model very different failure processes from metal plasticity (Dugdale 1960) to biocomposites damage (Gao 2006) and fracture in concrete (Hillerborg et al. 1976). We propose here to apply it to the periodic geometry of our molecular simulations and investigate if it can capture the behavior of CS1000.

The cohesive zone modeling introduces bridging forces between the crack faces that depend on the opening of the crack. The loading of the system takes place as follows (see Fig. 10). Prior to loading, in the initial state, there is no cohesive zone. Then, at the beginning of the loading, the crack tip starts to move ahead and the cohesive zone develops. When the opening at the end of the cohesive zone exceeds the maximum opening of the cohesive law, the unbridged crack starts to move ahead as well. Finally, when the crack tip coalesce at the periodic boundary, the cohesive zones keep transmitting stress across the crack until the unbridged crack coalesce. For the first regime before crack tip coalescence, the mechanical problem can be solved by introducing bridging forces in the periodic crack problem treated in the LEFM approach. For the second regime after coalescence, the mechanical problem is that of an elastic plate submitted to symmetric periodic tractions on its faces. This second mechanical problem can be solved in the Fourier space. We present both solutions hereafter.

We first consider the system before crack tip coalescence. The cohesive zone introduces bridging forces p behind the crack tip as a function of the opening $\delta\left(x\right)$ at position x. These bridging forces modify the pseudo-traction consistency Eq. 2 as follows:

$$\sigma^p\left(x\right) - 2\sum_{j=1}^{+\infty}\int_0^a K_{\sigma j}\left(x,u\right)\sigma^p\left(u\right)du + p\left(\delta\left(x\right)\right) = \Sigma \tag{13}$$

The crack opening $\delta\left(x\right)$ can be computed from the pseudo-tractions. Since the displacement discontinuity that leads to the crack opening is due to one of the subproblems only, we can use of the analytic formulation for a row of periodic collinear cracks (Tada et al. 2000). We have:

$$\delta\left(x\right) = \int_0^a K_\delta\left(x,u\right)\sigma^p\left(u\right)du \tag{14}$$

with

$$K_\delta\left(x,u\right) = \begin{cases} \frac{8}{\pi E'}\tanh^{-1}\left(\sqrt{\frac{1-\left(\cos\left(\frac{\pi a}{L_x}\right)/\cos\left(\frac{\pi u}{L_x}\right)\right)^2}{1-\left(\cos\left(\frac{\pi a}{L_x}\right)/\cos\left(\frac{\pi x}{L_x}\right)\right)^2}}\right) & \text{if } |x| \le u \\ \frac{8}{\pi E'}\coth^{-1}\left(\sqrt{\frac{1-\left(\cos\left(\frac{\pi a}{L_x}\right)/\cos\left(\frac{\pi u}{L_x}\right)\right)^2}{1-\left(\cos\left(\frac{\pi a}{L_x}\right)/\cos\left(\frac{\pi x}{L_x}\right)\right)^2}}\right) & \text{if } u < |x| \le a \end{cases} \tag{15}$$

Accordingly, the cohesive force distribution $p\left(\delta\left(x\right)\right)$ in Eq. 13 is a function of the pseudo-tractions $\sigma^p\left(x\right)$. Solving for the pseudo-tractions in Eq. 13, one can then access any quantity of interest (displacement/deformation, stress intensity etc.). As before, we followed the approach of Karihaloo et al. (1996) (Gauss–Legendre quadrature method with $\sigma^p\left(x\right)$ discretized at the integration points). However, the problem is no

more linear because of the cohesive law $p(\delta)$. We used an iterative Newton–Raphson method to solve the nonlinear problem. In addition, special attention must be paid to discretization with respect to the discontinuities of bridging forces to avoid integration and convergence errors. At each loading step, the length of the cohesive zone is adjusted so that the total stress intensity at the crack tip is zero.

After crack tip coalescence at the periodic boundaries, the mechanical problem becomes that of stacked periodic plates separated by cohesive zones which exert a load function of the distance between consecutive plates (Fig. 10). By symmetry, the stress and strain fields are even about the center of the unbridged crack. To solve this new mechanical problem, we consider the solution of Sneddon (1951) for an infinite plate loaded by even forces on its faces. The solution of Sneddon consists in solving the mechanical problem in the Fourier space. Applying a cosine Fourier transform to the equations of mechanical equilibrium in the absence of body forces gives:

$$\left(\frac{\partial^2}{\partial y^2} - \xi^2\right) G = 0$$
$$\text{with } G(\xi, y) = \int_0^\infty \chi(x, y) \cos(\xi x)\, dx \tag{16}$$

where χ is the Airy stress function. The function G replaces χ in the Fourier space and fully determines the stress, strain and displacement fields. In particular, the normal component of the stress in the vertical direction, the shear stress and the displacement in the vertical direction are:

$$\sigma_y(x, y) = -\frac{2}{\pi} \int_0^\infty \xi^2 G \cos(\xi x)\, d\xi \tag{17}$$

$$\tau_{xy}(x, y) = \frac{2}{\pi} \int_0^\infty \xi \frac{\partial G}{\partial y} \sin(\xi x)\, d\xi \tag{18}$$

$$u_y(x, y) = \frac{2}{\pi} \int_0^\infty \frac{1+\nu}{E} \left(\frac{1-\nu}{\xi^2} \frac{\partial^3 G}{\partial y^3} - (2-\nu) \frac{\partial G}{\partial y}\right) \cos(\xi x)\, d\xi \tag{19}$$

In the particular case of a plate, the solutions of Eq. 16 take the form:

$$G(\xi, y) = (A + B\xi y) \cosh(\xi y) + (C + D\xi y) \sinh(\xi y) \tag{20}$$

where A, B, C and D are constants that depend on the boundary conditions. We consider a plate submitted to an even vertical traction load $p(x)$ on its upper and lower faces ($y = L_y/2$ and $y = -L_y/2$, considering the middle of the plate as the origin). Introducing these boundary conditions in Eqs. 17 and 18 leads to the following values for the constants: $A = -\frac{\xi L_y \cosh(\xi L_y/2) + 2\sinh(\xi L_y/2)}{\xi L_y + \sinh(\xi L_y)} \frac{\widetilde{p}(\xi)}{\xi^2}$, $B = C = 0$ and $D = \frac{2\sinh(\xi L_y/2)}{\xi L_y + \sinh(\xi L_y)} \frac{\widetilde{p}(\xi)}{\xi^2}$ where $\widetilde{p}(\xi) = \int_0^\infty p(x) \cos(\xi x)\, dx$ is the cosine Fourier transform of the load p. The inverse transform is $p(x) = \frac{2}{\pi} \int_0^\infty \widetilde{p}(\xi) \cos(\xi x)\, d\xi$. Introducing the values of the constants into the expression of G (Eq. 16), we obtain the expression of the vertical displacement $u_y^{faces}(x) = u_y(x, y = b) = -u_y(x, y = -b)$ (Eq. 19) on the upper and lower faces:

$$u_y^{faces} = \frac{8}{\pi E'} \int_0^\infty \frac{\left(\sinh\left(\xi L_y/2\right)\right)^2}{\xi L_y + \sinh\left(\xi L_y\right)} \widetilde{p}(\xi) \frac{\cos(\xi x)}{\xi} d\xi \tag{21}$$

In our case, the load p is a periodic function of period L_x. Therefore, the cosine Fourier transforms can be replaced with Fourier series with the Fourier coefficients $\widetilde{p}_k = \frac{2}{L_x} \int_0^{\frac{L_x}{2}} p(x) \cos\left(\frac{2\pi k}{L_x} x\right) dx$. Equation 21 becomes:

$$u_y^{faces} = \frac{8}{\pi E'} \sum_{k=0}^{\infty} \frac{\left(\sinh\left(\pi k \frac{L_y}{L_x}\right)\right)^2}{2\pi k \frac{L_y}{L_x} + \sinh\left(2\pi k \frac{L_y}{L_x}\right)} \widetilde{p}_k \frac{\cos\left(\frac{2\pi k}{L_x} x\right)}{\frac{2\pi k}{L_x}} \tag{22}$$

Equation 22 gives the deformed configuration of a linear elastic plate under the action of an even symmetric periodic load on its faces. Owing to the cohesive law, the load p is a function of the opening δ of the crack, that is of the distance between two consecutive plates. The opening δ and the displacement of the boundaries $u_y(\pm b)$ are related according to: $\delta(x) = \delta_0 - 2 \cdot \left(u_y^{faces}(x) - u_y^{faces}(0)\right)$, where δ_0 is a parameter representing the opening at $x = 0$. The mechanical problem can be formulated in terms of a consistency equation that must be satisfied by the opening δ:

$$\delta(x) = \delta_0 - \frac{16}{\pi E'} \times \sum_{k=0}^{\infty} \frac{\left(\sinh\left(\pi k \frac{L_y}{L_x}\right)\right)^2}{2\pi k \frac{L_y}{L_x} + \sinh\left(2\pi k \frac{L_y}{L_x}\right)} \widetilde{p}_k \frac{\cos\left(\frac{2\pi k}{L_x} x\right) - 1}{\frac{2\pi k}{L_x}} \tag{23}$$

where $\widetilde{p}_k = \frac{2}{L_x} \int_0^{\frac{L_x}{2}} p(\delta(x)) \cos\left(\frac{2\pi k}{L_x} x\right) dx$ and $p(\delta(x))$ is the cohesive law. The opening function $\delta(x)$, which is the solution of Eq. 23, fully characterizes the mechanics of the system since one can then derive from it the full stress, strain and displacement fields. Except for linear cohesive laws, the problem of Eq. 23 is non linear and no simple analytic solution exists. In our work, we solve Eq. 23 by adopting a similar approach as was done previously for computing the doubly periodic crack problem with cohesive zones. That is, we use Gauss–Legendre method for integration of the Fourier coefficients $\widetilde{p}_k$ while the opening δ is discretized at the integration points. We solve Eq. 23 iteratively with a Newton-Raphson method. Doing so, we can solve the mechanical problem for a wide variety of cohesive laws, but the discretization must be adapted carefully from one law to another to avoid integration and convergence errors (due to discontinuities in the law for instance).

The relationship between the dimensionless strain $\Delta^* = 2\Delta/L_y$ and stress $\Sigma^* = \Sigma/E'$ depends not only on the geometric ratios $2a/L_x$ and L_y/L_x as in Eq. 7, but also on the cohesive law. As an example, we display in Fig. 11 the case of a plastic cohesive law, i.e., $p(\delta) = \sigma_{YS}$ for $\delta < \delta_{cr}$ with σ_{YS} the yield stress of the material. In Fig. 11, we show how the loading curve changes with the dimensionless ratio $\delta^*_{cr}/\sigma^*_{YS} = (2\delta_{cr}/L_x) / (\sigma_{YS}/E')$ which quantifies the degree of ductility of the plastic cohesive law. Alternatively, we can also relate this quantity to the ratio between the critical stress for an infinite body (K^*_{Ic}) and the yield stress (σ^*_{YS}) as follows: $\delta^*_{cr}/\sigma^*_{YS} = (2\pi a/L_x) \cdot \left(K^*_{Ic}/\sigma^*_{YS}\right)^2$. Accordingly, we expect a significant difference with LEFM at large values of $\delta^*_{cr}/\sigma^*_{YS}$. This is well illustrated in Fig. 11. For $\delta^*_{cr}/\sigma^*_{YS} \to 0$, the plastic cohesive zone model predicts the same loading curve as LEFM. But with increasing ductility ratio, the cohesive zone model introduces non linearity and ultimately a plastic plateau, so that the shape of the loading curve significantly differ from the LEFM prediction.

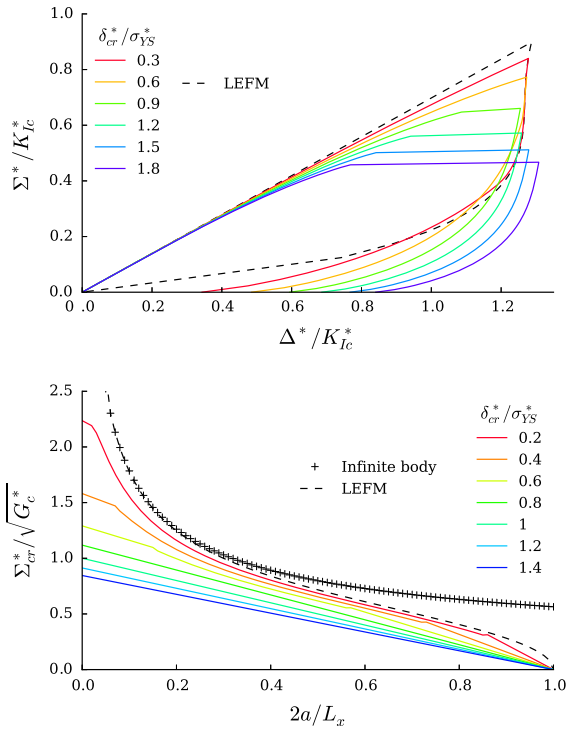

Fig. 11 Loading curves and critical as predicted with a plastic cohesive zone model for various ductility ratios $\delta^*_{cr}/\sigma^*_{YS}$. For the loading curves (*top*), we display the dimensionless reduced stress Σ^*/K^*_{Ic} as a function of the dimensionless reduced strain Δ^*/K^*_{Ic} (with the geometrical ratios $2a/L_x = 0.5$ and $L_y/L_x = 1$). The loading curve from LEFM is displayed for comparison. The cohesive zone model introduces non linearity and the loading curves deviates from LEFM predictions. Deviation from LEFM increases with ductility and a plateau appears that is characteristic of the plastic cohesive law. For the critical stress (*bottom*), we display the dimensionless reduced failure stress $\Sigma^*_{cr}/\sqrt{G^*_c}$ as a function of the crack size $2a/L_x$ (with the geometric ratio $L_y/L_x = 1$). For comparison, we also display the prediction of LEFM for the same periodic geometry and for a finite crack in an infinite body. The usual trend in $1/\sqrt{a}$ gradually evolves toward a linear trend with increasing ductility

In Fig. 11, we also show how the ductility ratio $\delta^*_{cr}/\sigma^*_{YS}$ affects the critical stress at failure. We display the dimensionless reduced failure stress $\Sigma^*_{cr}/\sqrt{G^*_c} = \Sigma^*_{cr}/\sqrt{\delta^*_{cr}\sigma^*_{YS}}$ as a function of the crack size $2a/L_x$ for $L_y/L_x = 1$. The cohesive zone approach suppresses the stress singularity, and, accordingly, at low $2a/L_x$, the critical stress converges to a finite value $\Sigma_{cr} = \sigma_{YS}$, i.e., $\Sigma^*_{cr}/\sqrt{G^*_c} = 1/\sqrt{\delta^*_{cr}/\sigma^*_{YS}}$. As for the loading curve, the predictions of the cohesive zone model converge to LEFM predictions for $\delta^*_{cr}/\sigma^*_{YS} \to 0$. But, sig-

nificant discrepancy appears with increasing ductility. In particular, the usual trend in $1/\sqrt{a}$ gradually evolves toward a linear trend. The limit case is when the cohesive zone extends over the whole uncracked body:

$$\frac{\Sigma_{cr}}{\sigma_{YS}} = 1 - \frac{2a}{L_x} \Rightarrow \frac{\Sigma^*_{cr}}{\sqrt{G^*_c}} = \left(1 - \frac{2a}{L_x}\right) \frac{1}{\sqrt{\delta^*_{cr}/\sigma^*_{YS}}} \tag{24}$$

3.4 Application of the cohesive zone analysis to molecular simulation results

We have shown in the previous section that cohesive zone models lead to significant changes in the loading curve and critical stress of the periodic system. The plastic cohesive zone illustrated in Fig. 11 is an example, but it does not captures the shape of the loading curve we obtained for the nanoporous polymer (Fig. 5). To capture the behavior of the nanoporous polymer, we considered a linear decreasing cohesive law instead: $p(\delta) = \sigma_{YS}(1 - \delta/\delta_{cr})$ for $\delta < \delta_{cr}$. We display in Fig. 12 the loading curves and critical stress trend predicted with this cohesive law for various ductility ratios $\delta^*_{cr}/\sigma^*_{YS}$. The quantities displayed in Fig. 12 are the same as in Fig. 11. Note, however, that we consider a higher range of values for the ductility ratio $\delta^*_{cr}/\sigma^*_{YS}$ since the linear cohesive law dissipates two times less energy than the plastic cohesive law ($G^*_c = \delta^*_{cr}\sigma^*_{YS}/2$). As a consequence, based on energy equivalence, the ductility ratios of Fig. 12 are scaled by a factor of two compared to the ratios in Fig. 11, whence the higher values.

In Fig. 12, the qualitative shape of the loading curves at high ductility ratios are quite consistent with the molecular simulation results for CS1000 (Fig. 5). The trend of the critical stress is similar to that obtained with a plastic cohesive law: in the limit $\delta^*_{cr}/\sigma^*_{YS} \to 0$ the critical stress converges to the LEFM prediction, while at large ductility, the critical stress depends linearly on the crack length, with a limit case:

$$\frac{\Sigma_{cr}}{\sigma_{YS}} = 1 - \frac{2a}{L_x} \Rightarrow \frac{\Sigma^*_{cr}}{\sqrt{G^*_c}} = \left(1 - \frac{2a}{L_x}\right) \sqrt{\frac{2}{\delta^*_{cr}/\sigma^*_{YS}}} \tag{25}$$

Equation 25 differs from Eq. 24 by a factor of 2 which arises from the difference in energy release with

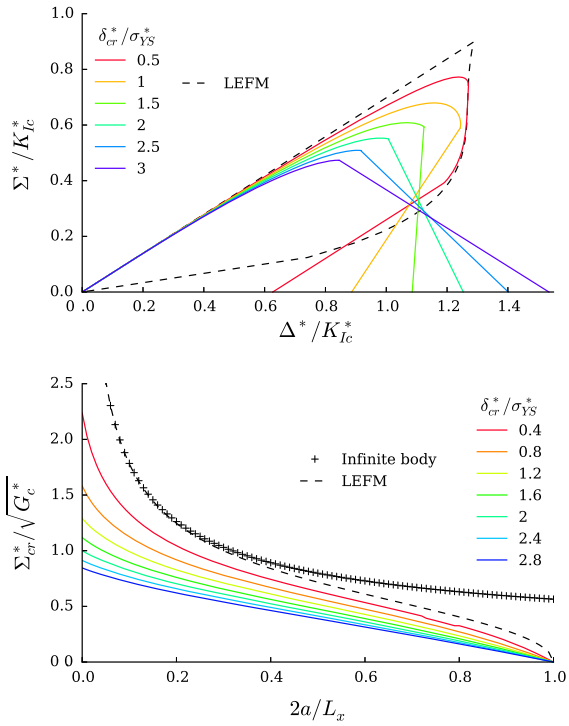

Fig. 12 Loading curves and critical as predicted with a linear cohesive zone model for various ductility ratios $\delta^*_{cr}/\sigma^*_{YS}$. The notations are the same as in Fig. 11. The loading curves deviates from LEFM prediction with increasing ductility and exhibit a linear decreasing branch at large ductility characteristic of the linear cohesive law. The usual trend of the critical stress in $1/\sqrt{a}$ evolves toward a linear trend at high ductility

the plastic cohesive law. We evaluated the trend of the critical stress from the results of molecular simulation of CS1000. We display in Fig. 13 the critical stresses for the various CS1000 systems simulated. Figure 13 shows that the critical stress obtained by molecular simulation follow a linear trend in a limited range of crack length ($0.2 < 2a_0/L_x < 0.6$). Note that the systems considered in Fig. 13 have different geometrical ratios L_y/L_x which is not accounted for in this analysis. A major consequence is that the dimensionless ductility ratio $\delta^*_{cr}/\sigma^*_{YS}$ differ from one system to another. But, in raw units (case of Fig. 13) the effect of L_y/L_x vanishes with increasing ductility ratio as the critical stress approaches the limit case (Eq. 25). The range of the linear trend ($0.2 < 2a_0/L_x < 0.6$) is not wide enough to characterize the degree of ductility of the cohesive law. Assuming that the linear relation applies (Eq. 25), the y-intercept of the linear trend in Fig. 13 is the yield stress σ_{YS}. Doing so, we obtain $\sigma_{YS} = 20$ GPa, which com-

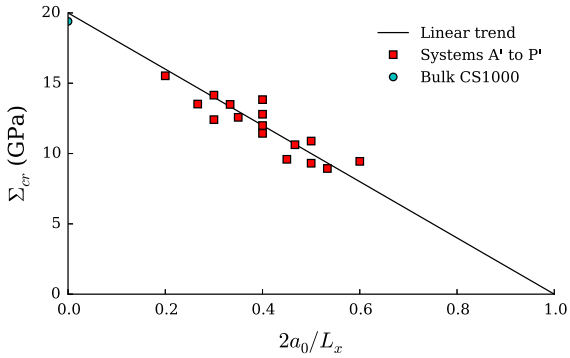

Fig. 13 Trend between the critical stress Σ_{cr} and the reduced crack length $2a_0/L_x$ for all the CS1000 systems considered

pares well with the yield stress estimated by molecular simulation of bulk CS1000 (19.4 GPa). Accordingly, the linear trend is valid up to small crack length which is characteristic of a high ductility ratio ($\delta^*_{cr}/\sigma^*_{YS} > 2$).

The analysis of the loading curve shape and critical stress confirms that the linear cohesive zone model is well adapted to model the behavior of CS1000.We calibrated the value of δ_{cr} to capture the loading curves from molecular simulations. We found that with $\delta_{cr} = 18.5$ Å the cohesive zone model captures reasonably well the mechanical responses of all the CS1000 systems considered. As an illustration, we display in Fig. 14 the loading curves for the three CS1000 systems of Fig. 4 along with the predictions from the linear cohesive zone model. In the framework of the cohesive model, the energy dissipated during fracture is concentrated in the cohesive zone and the critical energy release rate G_c can be obtained by integration of the cohesive law (Eq. 12). Thus, with the linear cohesive law, we have: $G_c = \delta_{cr}\sigma_{YS}/2 = 18.5$ N/m. Alternatively, we can compute G_c by integrating the loading curves from molecular simulation (Eq. 11). Unlike the case of α-cristobalite, this estimation is valid here since crack propagation is stable for CS1000. We obtain $G_c = 19.5 \pm 3.2$ N/m which is consistent with the value obtained from the cohesive law. In addition, no particular correlation is found between the energy release rates and the system size. If the process zone size was larger than the system size, we would observe that G_c increases with the system size up to an asymptotic value which is the relevant one at larger scales. Here, the high degree of cross-linking of CS1000 strongly limits the process zone size to the nanometer scale.

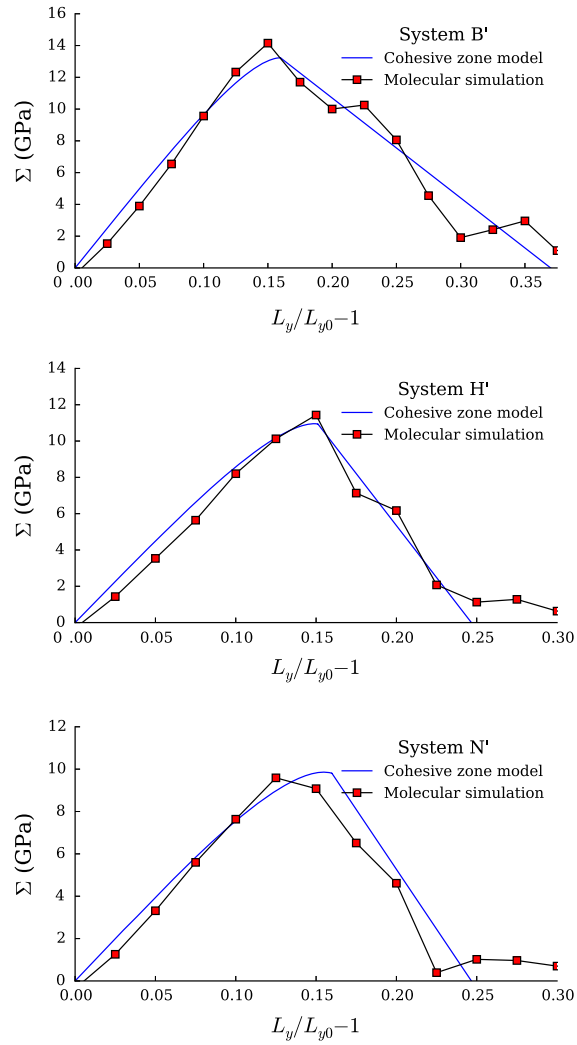

Fig. 14 Loading curves from molecular simulations compared with the cohesive model predictions for the three systems of Fig. 4

4 Conclusion

A careful analysis of molecular simulations of material fracture failure, in which we pay a special attention to the size effects, shows that usual LEFM predictions are still valid if the process zone size is small at the scale of molecular simulations. We illustrate this situation for a silica crystal, α-cristobalite, for which the process zone is only a few atoms large. Provided that boundary conditions are accounted for (periodic boundaries in our work), LEFM captures correctly the global material behavior (remote stress and average strain). In particular, one can directly estimate mate-

rial fracture properties, such as toughness, from molecular simulation. In contrast, when the process zone occupies a significant fraction of the molecular system, LEFM fails to predict the mechanical behavior. We illustrate this second situation with the example of a nanoporous polymer, CS1000, for which the process zone is about one order of magnitude larger than that of α-cristobalite. LEFM fails to predict the behavior of CS1000 both quantitatively and qualitatively: the LEFM scaling between critical stress and crack size (inverse square root) becomes linear, the stability of CS1000 failure does not follow LEFM analysis, and LEFM estimates of toughness from critical stress is not consistent with the total energy released during failure. To overcome the inherent limitations of LEFM in presence of large scale yielding, we develop an alternative analysis which includes cohesive zone models at the crack tips. Provided the cohesive law is well adapted, we recovered all the features of the mechanical behavior of CS1000 within this framework. From the cohesive law, one can then easily recover the macroscopic toughness and anticipate the mechanical behavior at larger scales. Thus, our analysis with cohesive zone models offers the possibility to upscale fracture properties from molecular simulation even with large yielding at the scale of the molecular system. It should be noted however that, the approach is limited by the size of the molecular system simulated since the process zone cannot extend further. The process zone size is on the order of the square of the ratio between toughness and yield stress. Thus, estimating this ratio is critical to know whether or not the scale of molecular simulations is relevant, and to decide what kind of analysis to perform.

Acknowledgments Funding for this work through the X-Shale project enabled through MIT's Energy Initiative, with sponsorship provided by Shell and Schlumberger, is greatly appreciated.

References

Abraham FF, Broughton J (1998) Large-scale simulations of brittle and ductile failure in fcc crystals. Comput Mater Sci 10(1):1–9

Abraham FF, Walkup R, Gao H, Duchaineau M, De La Rubia TD, Seager M (2002) Simulating materials failure by using up to one billion atoms and the world's fastest computer: work-hardening. Proc Natl Acad Sci 99(9):5783–5787

Allen MP, Tildesley DJ (1989) Computer simulation of liquids. Oxford University Press, Oxford

Anderson TL (2005) Fracture mechanics: fundamentals and applications. CRC Press, Boca Raton

Ashby MF (2005) Materials selection in mechanical design, 3rd edn. Butterworth-Heinemann, Oxford

Barenblatt GI (1962) The mathematical theory of equilibrium cracks in brittle fracture. Adv Appl Mech 7(1):55–129

Bazant ZP (1984) Size effect in blunt fracture: concrete, rock, metal. J Eng Mech 110(4):518–535

Belytschko T, Xiao S, Schatz G, Ruoff R (2002) Atomistic simulations of nanotube fracture. Phys Rev B 65(23):235,430

Bilby B, Cottrell A, Swinden K (1963) The spread of plastic yield from a notch. Proc R Soc Lond Ser A Math Phys Sci 272(1350):304–314

Bouchbinder E, Fineberg J, Marder M (2010) Dynamics of simple cracks. Ann Rev Condens Matter Phys 1(1):371–395

Buehler MJ, Gao H (2006) Dynamical fracture instabilities due to local hyperelasticity at crack tips. Nature 439(7074):307–310

Buehler MJ, van Duin AC, Goddard WA III (2006) Multiparadigm modeling of dynamical crack propagation in silicon using a reactive force field. Phys Rev Lett 96(9):095,505

Buehler MJ, Tang H, van Duin AC, Goddard WA III (2007) Threshold crack speed controls dynamical fracture of silicon single crystals. Phys Rev Lett 99(16):165,502

Chenoweth K, Cheung S, Van Duin AC, Goddard WA, Kober EM (2005) Simulations on the thermal decomposition of a poly (dimethylsiloxane) polymer using the reaxff reactive force field. J Am Chem Soc 127(19):7192–7202

Cheung K, Yip S (1994) A molecular-dynamics simulation of crack-tip extension: the brittle-to-ductile transition. Modell Simul Mater Sci Eng 2(4):865

de Celis B, Argon AS, Yip S (1983) Molecular dynamics simulation of crack tip processes in alpha-iron and copper. J Appl Phys 54(9):4864–4878

Downs R, Palmer D (1994) The pressure behavior of a-cristobalite. Am Miner 79:9–14

Dugdale D (1960) Yielding of steel sheets containing slits. J Mech Phys Solids 8(2):100–104

Frenkel D, Smit B (2002) Understanding molecular simulation: from algorithms to applications. Academic press, London

Gao H (2006) Application of fracture mechanics concepts to hierarchical biomechanics of bone and bone-like materials. Int J Fract 138(1–4):101–137

Garrison W Jr, Moody N (1987) Ductile fracture. J Phys Chem Solids 48(11):1035–1074

Gumbsch P, Zhou S, Holian B (1997) Molecular dynamics investigation of dynamic crack stability. Phys Rev B 55(6):3445

Hillerborg A, Modéer M, Petersson PE (1976) Analysis of crack formation and crack growth in concrete by means of fracture mechanics and finite elements. Cem Concr Res 6(6):773–781

Holian BL, Ravelo R (1995) Fracture simulations using large-scale molecular dynamics. Phys Rev B 51(17):11,275

Holland D, Marder M (1998) Ideal brittle fracture of silicon studied with molecular dynamics. Phys Rev Lett 80(4):746

Holland D, Marder M (1999) Cracks and atoms. Adv Mater 11(10):793–806

Hutchinson J (1968) Singular behaviour at the end of a tensile crack in a hardening material. J Mech Phys Solids 16(1):13–31

Isida M, Ushijima N, Kishine N (1981) Rectangular plates, strips and wide plates containing internal cracks under various boundary conditions. Trans Jpn Soc Mech Eng Part A 47:27–35

Jain SK, Pellenq RJM, Pikunic JP, Gubbins KE (2006) Molecular modeling of porous carbons using the hybrid reverse Monte Carlo method. Langmuir 22(24):9942–9948

Karihaloo B, Wang J (1997) On the solution of doubly periodic array of cracks. Mech Mater 26(4):209–212

Karihaloo B, Wang J, Grzybowski M (1996) Doubly periodic arrays of bridged cracks and short fibre-reinforced cementitious composites. J Mech Phys Solids 44(10):1565–1586

Kermode J, Albaret T, Sherman D, Bernstein N, Gumbsch P, Payne M, Csányi G, De Vita A (2008) Low-speed fracture instabilities in a brittle crystal. Nature 455(7217):1224–1227

Kermode J, Ben-Bashat L, Atrash F, Cilliers J, Sherman D, De Vita A (2013) Macroscopic scattering of cracks initiated at single impurity atoms. Nat Commun 4:2441

Kramer E, Berger L (1990) Fundamental processes of craze growth and fracture. In: Kausch HH (ed) Crazing in polymers vol. 2, advances in polymer science, vol 91/92, vol 2. Springer, Berlin, pp 1–68

Kröner E (1967) Elasticity theory of materials with long range cohesive forces. Int J Solids Struct 3(5):731–742

Langer J, Lobkovsky AE (1998) Critical examination of cohesive-zone models in the theory of dynamic fracture. J Mech Phys Solids 46(9):1521–1556

Lawn BR (1983) Physics of fracture. J Am Ceram Soc 66(2):83–91

Lucas J, Moody N, Robinson S, Hanrock J, Hwang R (1995) Determining fracture toughness of vitreous silica glass. Scr Metall Mater 32(5):743–748

Marder M (2004) Effects of atoms on brittle fracture. Int J Fract 130(2):517–555

Marder M, Gross S (1995) Origin of crack tip instabilities. J Mech Phys Solids 43(1):1–48

Mattoni A, Colombo L, Cleri F (2005) Atomic scale origin of crack resistance in brittle fracture. Phys Rev Lett 95(11):11,5501

Miller R, Tadmor E, Phillips R, Ortiz M (1998) Quasicontinuum simulation of fracture at the atomic scale. Modell Simul Mater Sci Eng 6(5):607

Nakano A, Kalia RK, Vashishta P (1994) Growth of pore interfaces and roughness of fracture surfaces in porous silica: Million particle molecular-dynamics simulations. Phys Rev Lett 73(17):2336

Nazmus Sakib A, Adnan A (2012) On the size-dependent critical stress intensity factor of confined brittle nanofilms. Eng Fract Mech 86:13–22

Oh ES, Walton JR, Slattery JC (2006) A theory of fracture based upon an extension of continuum mechanics to the nanoscale. J Appl Mech 73(5):792–798

Pérez R, Gumbsch P (2000) Directional anisotropy in the cleavage fracture of silicon. Phys Rev Lett 84(23):5347

Plimpton S (1995) Fast parallel algorithms for short-range molecular dynamics. J Comput Phys 117(1):1–19

Pugno NM, Ruoff RS (2004) Quantized fracture mechanics. Philos Mag 84(27):2829–2845

Rice JR, Thomson R (1974) Ductile versus brittle behaviour of crystals. Philos Mag 29(1):73–97

Rottler J (2009) Fracture in glassy polymers: a molecular modeling perspective. J Phys Condens Matter 21(46):463,101

Rottler J, Barsky S, Robbins MO (2002) Cracks and crazes: on calculating the macroscopic fracture energy of glassy polymers from molecular simulations. Phys Rev Lett 89(14):148,304

Sauer J, Hara M (1990) Effect of molecular variables on crazing and fatigue of polymers. In: Kausch HH (ed) Crazing in polymers vol 2, advances in polymer science, vol 91/92. Springer, Berlin, pp 69–118

Sinclair J (1975) The influence of the interatomic force law and of kinks on the propagation of brittle cracks. Philos Mag 31(3):647–671

Smith TL (1958) Dependence of the ultimate properties of a GR-S rubber on strain rate and temperature. J Polym Sci 32(124):99–113

Sneddon IN (1951) Fourier transforms. Dover, New York

Swiler T (1994) Atomic-scale dynamic processes in the brittle fracture of silica. In: PhD thesis, University of Florida

Swiler TP, Simmons JH, Wright AC (1995) Molecular dynamics study of brittle fracture in silica glass and cristobalite. J Non-cryst Solids 182(1):68–77

Tada H, Paris PC, Irwin GR (2000) The stress analysis of cracks handbook. American Society of Mechanical Engineers, New York

Thomson R, Hsieh C, Rana V (1971) Lattice trapping of fracture cracks. J Appl Phys 42(8):3154–3160

Van Duin AC, Dasgupta S, Lorant F, Goddard WA (2001) Reaxff: a reactive force field for hydrocarbons. J Phys Chem A 105(41):9396–9409

Van Duin AC, Strachan A, Stewman S, Zhang Q, Xu X, Goddard WA (2003) Reaxffsio reactive force field for silicon and silicon oxide systems. J Phys Chem A 107(19):3803–3811

Ward IM, Sweeney J (2012) Mechanical properties of solid polymers. Wiley, New York

Watanabe K, Atsumi A (1972) Infinite row of parallel cracks in a strip. Int J Eng Sci 10(2):173–184

Zhang S, Zhu T, Belytschko T (2007) Atomistic and multiscale analyses of brittle fracture in crystal lattices. Phys Rev B 76(9):094,114

Zhou S, Lomdahl P, Thomson R, Holian B (1996) Dynamic crack processes via molecular dynamics. Phys Rev Lett 76(13):2318